

Filamentation and damage in fused silica induced by tightly focused femtosecond laser pulsesA. Couairon,¹ L. Sudrie,² M. Franco,² B. Prade,² and A. Mysyrowicz²¹*Centre de Physique Théorique, École Polytechnique, CNRS UMR 7644, F-91128, Palaiseau Cedex, France*²*Laboratoire d'Optique Appliquée, École Nationale Supérieure des Techniques Avancées-École Polytechnique, CNRS UMR 7639, F-91761 Palaiseau Cedex, France*

(Received 8 April 2004; revised manuscript received 24 June 2004; published 31 March 2005)

We investigate experimentally and numerically the damage tracks induced by tightly focused (NA=0.5) infrared femtosecond laser pulses in the bulk of a fused silica sample. Two types of irreversible damage are observed. The first damage corresponds to a permanent change of refractive index without structural modifications (type I). It appears for input pulse energies beyond $0.1 \mu\text{J}$. It takes the form of a narrow track extending over more than $100 \mu\text{m}$ at higher input powers. It is attributed to a change of the polarizability of the medium, following a filamentary propagation which generates an electron-hole plasma through optical field ionization. A second type of damage occurs for input pulse energies beyond $0.3 \mu\text{J}$ (type II). It takes the form of a pear-shaped structural damage associated with an electron-ion plasma triggered by avalanche. The temporal evolution of plasma absorption is studied by pump-probe experiments. For type I damage, a fast electron-hole recombination is observed. Type II damage is linked with a longer absorption.

DOI: 10.1103/PhysRevB.71.125435

PACS number(s): 79.20.Ds, 61.80.Ba, 72.20.Jv, 42.65.Jx

I. INTRODUCTION

The controlled deposition of laser energy in transparent solids is of crucial importance for several applications such as micromachining of optical materials,¹⁻⁴ biomedical technologies,⁵ or three-dimensional optical data storage.^{6,7} Laser damage often constitutes a limiting factor for the development of these applications because it can prevent the transmission of energy in the bulk of transparent media. The understanding of the mechanisms responsible for damage in dielectrics is therefore the subject of intense investigation, while the structural modifications induced by focusing femtosecond laser pulses are currently applied to the fabrication of optical devices such as waveguides in glasses,^{2,8} gratings,^{9,10} fiber gratings,¹¹ couplers,³ or photonic crystals.¹²

In this paper, the propagation of femtosecond laser pulses in fused silica is investigated experimentally and numerically, under tight focusing conditions. In this case, unlike in surface damage experiments,¹³ the laser pulses propagate in the bulk of the sample and cause permanent damage to the material without ablating the surface. Fundamental aspects of laser-dielectric interaction are studied, in particular the effect of basic processes occurring in the presence of a high laser field such as photoionization, free-carrier absorption, carrier-carrier interaction, as well as self-induced effects such as self-phase modulation or self-focusing that can dramatically affect the propagation. Inspection of the damage tracks provides useful diagnostics on the pulse propagation in the medium. These experimental observations are compared with numerical results from a code that describes the propagation of the laser pulse coupled with the evolution of the electron plasma generated by avalanche and photoionization. Both experimental and numerical results show that the laser pulse propagates in the form of a filament. The local intensity and the density of the plasma generated during the propagation of the pulse can be obtained accurately by means of comparisons of the damage tracks with isodensity contours of the electron density computed numerically.

The outline of this paper is the following: First, we study the shift toward the laser of the damage caused along the propagation axis when the energy of the incident laser pulse varies. From this observation, the self-focusing of the laser beam by the optical Kerr effect is quantitatively estimated. Measurements of the transmission of the pulses as a function of the incident energy are then presented and compared with the results of numerical simulations. Thereafter, we analyze the tracks of permanent damage. Comparisons of these tracks with the numerical results allows us to infer the electron density corresponding to the threshold of permanent damage. This paper ends with pump-probe measurements which make it possible to follow the temporal evolution of plasma absorption. A maximum value for the density of the plasma generated in the medium is given.

II. EXPERIMENTAL SETUP

We have used two types of laser sources. The first source is a cw-pumped regenerative Ti:S oscillator-amplifier laser system (Coherent RegA) delivering a train of pulses of $2 \mu\text{J}$ energy at 800 nm with a duration of 160 fs (FWHM) and a repetition rate of 200 kHz . The second laser source is an experimental chain developed in our laboratory. It is a CPA Ti:sapphire laser consisting of an oscillator, a regenerative amplifier, and two power amplifiers. This chain is able to deliver pulses with a central wavelength of 800 nm , an energy of 7 mJ , and a duration of 50 fs at a repetition rate of 1 kHz .

The laser beam is focused in the bulk of a transparent solid medium. The diagram of Fig. 1 gives a simplified overall picture of the experimental setup. The sample and the focusing objective are mounted on computer-controlled translation stages with micrometric precision. The entrance face of the sample is perpendicular to the propagation axis z . The sample can be moved along three axes x , y , z by three stepping motors. A camera placed after the sample enables us

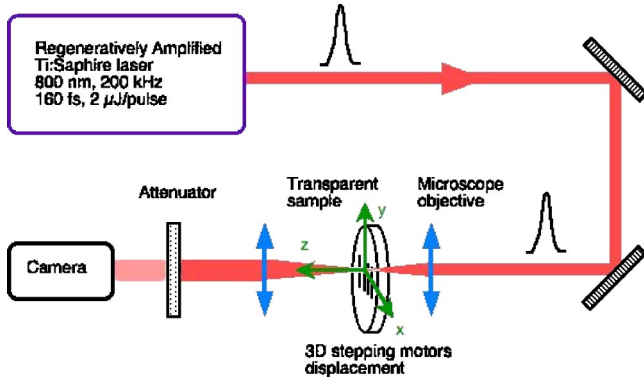


FIG. 1. Experimental setup.

to control the depth of the beam focusing. In order to characterize the absorption of the pulses, we also measured the transmitted power.

The spatial profile of the beam at the linear focus is a significant parameter that we measured to specify the focusing conditions, as well as to characterize the optical elements used and their performances. The focusing geometry is characterized by the beam waist measured in air for a beam with low intensity. Table I gives the parameters of the microscope objectives used. The waist at the focus of each objective was recorded with an infrared camera, using a collecting objective of magnification 40 \times . The intensity profiles obtained from the images were fitted by Gaussians and their waist, defined as the width at $1/e^2$ maximum of the intensity, are given for each objective in Table I.

In the following, we concentrate on results obtained with the objective 20 \times with NA=0.5 for which a waist $w_f = 1.1 \mu\text{m}$ was measured.

III. NUMERICAL SIMULATIONS

The numerical code used in this study relies on the physical model developed for the propagation of an intense pulse in fused silica,^{14,15} noble gases or air,^{16,17} and liquids.^{18–20}

We model the linearly polarized beam with cylindrical symmetry around the propagation axis z by the envelope \mathcal{E} of the electric field \mathbf{E} , written as $\mathbf{E} = \text{Re}[\mathcal{E} \exp(ikz - i\omega_0 t)]$, where $k = n_0 \omega_0 / c$ and ω_0 are the wave number and frequency of the carrier wave, respectively, and $n_0 = 1.45$ for fused silica. The input pulses were modeled by Gaussians with energy E_{in} , a temporal FWHM duration of 160 fs (temporal half-width $t_p = 136$ fs) or 50 fs ($t_p = 42$ fs), an input power $P_{\text{in}} = E_{\text{in}} / t_p \sqrt{\pi/2}$, and intensity $\mathcal{E}_0^2 = 2P_{\text{in}} / \pi w_0^2$

$$\mathcal{E}(r, t, 0) = \mathcal{E}_0 \exp\left(-\frac{r^2}{w_0^2} - \frac{t^2}{t_p^2} - i\frac{kr^2}{2f}\right). \quad (1)$$

They exhibit a transverse waist $w_0 = w_f(1 + d^2/z_f^2)^{1/2}$, where $w_f = 1 \mu\text{m}$ is the beam waist, $z_f = \pi w_f^2 n_0 / \lambda_0 = 5.7 \mu\text{m}$ the

TABLE I. Numerical aperture and beam waist measured with a low intensity femtosecond laser at 800 nm for various objectives.

Magnification	2.5 \times	4 \times	10 \times	20 \times	40 \times
NA	0.07	0.12	0.25	0.5	0.65
waist $w_f(\mu\text{m})$	4.8	3.5	1.8	1.1	0.7

Rayleigh length, and $f = d + z_f^2/d$ the curvature of the wave at the distance d from the linear focus (we start our simulations at $d = 75 \mu\text{m}$ from the focus).

Two coupled equations describe the evolution of the envelope of the electric field and the electron density. The scalar envelope $\mathcal{E}(r, t, z)$ is assumed to be slowly varying in time. It evolves along the propagation axis z according to the nonlinear envelope equation,²¹ expressed in the frequency domain corresponding to the retarded time $t \equiv t_{\text{lab}} - z/v_g$

$$\hat{U} \frac{\partial \hat{\mathcal{E}}}{\partial z} = i \left[\frac{\nabla_{\perp}^2}{2k} + \left(\hat{U} + \frac{\hat{L}}{2k} \right) \hat{L} \right] \hat{\mathcal{E}} + iN(\hat{\mathcal{E}}), \quad (2)$$

where $v_g \equiv \partial\omega/\partial k|_{\omega_0}$ denotes the group velocity, $\hat{U}(\omega) \equiv 1 + \omega/kv_g$, and $\hat{L}(\omega) \equiv n(\omega)\omega/c - k - \omega/v_g$. Equation (2) accounts for diffraction in the transverse plane, group velocity dispersion, and high-order dispersive terms exactly computed by means of a Sellmeier dispersion relation for the refraction index $n(\omega)$ of silica in the form

$$n^2(\lambda) - 1 = \sum_{m=1}^3 B_m \frac{\lambda^2}{\lambda^2 - \lambda_m^2}, \quad (3)$$

where $B_1 = 0.6962$, $B_2 = 0.4079$, $B_3 = 0.8975$, $\lambda_1 = 0.0684 \mu\text{m}$, $\lambda_2 = 0.1162 \mu\text{m}$, $\lambda_3 = 9.8962 \mu\text{m}$. The second-order group velocity dispersion coefficient computed from this dispersion relation at 800 nm is $k'' \equiv \partial^2 k / \partial \omega^2|_{\omega_0} = 361 \text{ fs}^2/\text{cm}$. Describing the dispersive properties of the medium is important to obtain correct spectral and temporal evolution of the laser pulse. It was shown recently that these properties must be taken into account to obtain a correct physical description of supercontinuum generation in condensed media.^{22,23} Equation (2) accounts for space-time focusing (due to the presence of the operator \hat{U} in front of $\partial/\partial z$; see Refs. 21 and 24), and various nonlinear effects including optical Kerr effect with a nonlocal term corresponding to delayed Raman-Kerr optical shock response,^{25,26} self-steepening, plasma absorption, plasma defocusing and energy absorption due to photoionization. The operator $N(\hat{\mathcal{E}})$ in Eq. (2) denotes the time-Fourier transform of these nonlinear terms

$$N(\mathcal{E}) = k_0 n_2 T^2 \left[(1 - f_R) |\mathcal{E}(t)|^2 + f_R \int_{-\infty}^t d\tau R(\tau - t) |\mathcal{E}(\tau)|^2 \right] \mathcal{E}(t) - \frac{\sigma}{2} (1 + i\omega_0 \tau_c) \rho \mathcal{E} - \frac{T W_{\text{PI}}(|\mathcal{E}|^2) U_i}{2 |\mathcal{E}|^2} \mathcal{E}. \quad (4)$$

The operator $T \equiv 1 + (i/\omega_0)(\partial/\partial t)$ in front of the Kerr term is responsible for the self-steepening of the pulse.^{24,27,28} Self-focusing related to the Kerr effect occurs for pulses with P_{in} above $P_{\text{cr}} = 1.98 \text{ MW}$. This critical value was measured experimentally as indicated below, and corresponds to the nonlinear refraction index of fused silica $n_2 = 3.54 \times 10^{-16} \text{ cm}^2/\text{W}$ which we used in our simulations. It is in agreement with Ref. 29 ($n_2 = 3.75 \times 10^{-16} \text{ cm}^2/\text{W}$, $P_{\text{cr}} = 1.72 \text{ MW}$). From Refs. 23 and 25, the response function that accounts for the delayed Raman contribution in the Kerr effect may be written as

$$R(t) = \Omega^2 \tau_s \exp\left(-\frac{t}{\tau_d}\right) \times \sin\left(\frac{t}{\tau_s}\right),$$

with the characteristic times $\tau_d = 32$ fs and $\tau_s = 12$ fs (see Ref. 23), $\Omega^2 = \tau_s^{-2} + \tau_d^{-2}$, and fraction $f_R = 0.18$.

For plasma absorption, the cross section for inverse bremsstrahlung follows the Drude model^{30–32} and reads

$$\sigma = \frac{ke^2}{n_0^2 \omega_0^2 \epsilon_0 m} \times \frac{\omega_0 \tau_c}{1 + \omega_0^2 \tau_c^2}. \quad (5)$$

Below, we indicate how we inferred the value of the momentum transfer collision time τ_c from transmission measurements. This step is crucial to correctly describe the multiplication of electrons, with density ρ , inducing the damage of the material. The collision time also enters into the plasma defocusing term ($-i\sigma\omega_0\tau_c\rho\mathcal{E}/2$) in Eq. (4). For usual materials $\tau_c \gg \omega_0^{-1} = 4.2 \times 10^{-16}$ s, plasma absorption is a decreasing function while plasma defocusing is an increasing function of τ_c . The collision time therefore characterizes the balance between plasma absorption and plasma defocusing.

The strong focusing leads to high intensities and therefore, the multiphoton ionization rate generally used in this model^{15,23,33} has been changed into a photoionization rate W_{PI} derived from the general Keldysh formula³⁴ in the equation describing the evolution of the electron density. To be consistent, in the evolution equation (4) for the electric field, the last term describes photoabsorption, i.e., the energy losses due to optical field ionization instead of the standard multiphoton absorption term.

The evolution equation for the electron density reads

$$\frac{\partial \rho}{\partial t} = W_{PI}(|\mathcal{E}|) + \frac{\sigma}{U_i} \rho |\mathcal{E}|^2 - \frac{\rho}{\tau_r}. \quad (6)$$

The first term on the right-hand side of Eq. (6) describes the photoionization contribution to free-electron generation, involving transition from the valence band to the conduction band,^{35,36} through the gap potential $U_i = 9$ eV in silica. The second term accounts for avalanche ionization. The third term represents electron recombination with a characteristic mean time $\tau_r = 150$ fs in fused silica.³⁷

At this point, we make the following comment concerning the concept of plasma. Many experiments are concerned with the damage threshold at the sample surface. The plasma threshold is then associated with ablation of matter in the form of a plume. The corresponding plasma consists of electrons and ions. In the bulk damage study we address here, the first type of generated plasma corresponds to electrons and holes produced by multiphoton band-to-band transitions. Eventually, at increasing laser intensities, this electron-hole plasma will evolve into an electron-ion plasma. The triggering mechanism is the interaction of the laser pulse with the electron-hole plasma by inverse bremsstrahlung [avalanche ionization; see the second term in Eq. (6)]. In this paper, we only consider a situation close to the threshold for avalanche breakdown. We further approximate the electron-hole plasma recombination by a single exponential law with the decay constant $\tau_r = 150$ fs.³⁷ Such a situation occurs when plasma recombination is dominated by fast trapping of carriers into

localized states below the band gap. The rate equation (6) was recently revisited by Rethfeld and co-workers.^{38,39} They have shown that the physics of the avalanche process may be more precisely reproduced by using a set of rate equations describing the changes in the density of free electrons at various energy levels in the conduction band.

Following Keldysh's³⁴ formulation for the PI rate W_{PI} , we define the adiabaticity parameter for solids $\gamma = \omega_0 \sqrt{m} U_i / e \mathcal{E}$, where $m = 0.64 m_e$ (see Ref. 40) denotes the reduced mass of the electron and the hole; γ is equal to unity for an intensity $I = 3.5 \times 10^{13}$ W/cm². In our simulations, I reaches 5×10^{13} W/cm² near the focus for $E_{in} = 1$ μ J. Therefore, the PI rate can neither be reduced to the tunnel formula valid for $\gamma \ll 1$ nor to the multiphoton rate prevailing for weak fields $\gamma \gg 1$. The full Keldysh formulation for the PI rate reads

$$W_{PI}(|\mathcal{E}|) = \frac{2\omega_0}{9\pi} \left(\frac{\omega_0 m}{\hbar \sqrt{\Gamma}} \right)^{3/2} Q(\gamma, x) \exp(-\alpha \langle x+1 \rangle), \quad (7)$$

where

$$\Gamma = \frac{\gamma^2}{1 + \gamma^2}, \quad \Xi = \frac{1}{1 + \gamma^2},$$

$$Q(\gamma, x) = \sqrt{\frac{\pi}{2K(\Xi)}} \times \sum_{n=0}^{\infty} \exp(-n\alpha) \Phi(\sqrt{\beta(n+2\nu)}),$$

$$\alpha = \pi \frac{K(\Gamma) - E(\Gamma)}{E(\Xi)}, \quad \beta = \frac{\pi^2}{4K(\Xi)E(\Xi)},$$

$$x = \frac{2}{\pi} \frac{U_i}{\hbar \omega_0} \frac{E(\Xi)}{\sqrt{\Gamma}}, \quad \nu = \langle x+1 \rangle - x, \quad (8)$$

where $\langle \cdot \rangle$ denotes the integer part, K and E denote the complete elliptic integral of the first and second kind, respectively, and Φ the Dawson function $\Phi(z) = \int_0^z \exp(y^2 - z^2) dy$. Equations (7) and (8) are nothing but Keldysh's formulation written with complete elliptic integral functions as defined in Ref. 41. As a result, Eq. (39) in Ref. 34 contains $K(X^{1/2})$ and $E(X^{1/2})$ where Eqs. (7) and (8) contain $K(X)$ and $E(X)$. In agreement with these definitions and with Ref. 42, our quantity β is divided by 4, whereas the corresponding quantity in Ref. 34 is divided by 2.

Figure 2 shows the ionization rate W_{PI} for silica as a function of the laser intensity. It approaches asymptotically Keldysh's multiphoton rate (dotted curve) and tunnel ionization rate (dash-dotted curve) at the extreme limits of weak and strong fields. For weak fields, Keldysh's theory coincides with the multiphoton ionization rate $W_{MPI} = \sigma_6 I^6 \rho_{at}$ shown by the dashed line, where $\sigma_6 = 9.6 \times 10^{-70}$ s⁻¹ cm¹²/W⁶ denotes the coefficient for silica and $\rho_{at} = 2.1 \times 10^{22}$ cm⁻³, the background atom density. At $I = 3.5 \times 10^{13}$ W/cm² ($\gamma = 1$), $W_{MPI} = 3.7 \times 10^{34}$ cm⁻³ s⁻¹ clearly overestimates the PI rate $W_{PI} = 1.6 \times 10^{32}$ cm⁻³ s⁻¹ by two orders of magnitude. This is the reason why σ_6 is taken to be smaller in the literature ($\sigma_6 = 1.5 \times 10^{-71}$ s⁻¹ cm¹²/W⁶; see Ref. 36), but larger values are also used ($\sigma_6 = 3 \times 10^{-67 \pm 0.9}$ s⁻¹ cm¹²/W⁶; Ref. 43). Our simulations could re-

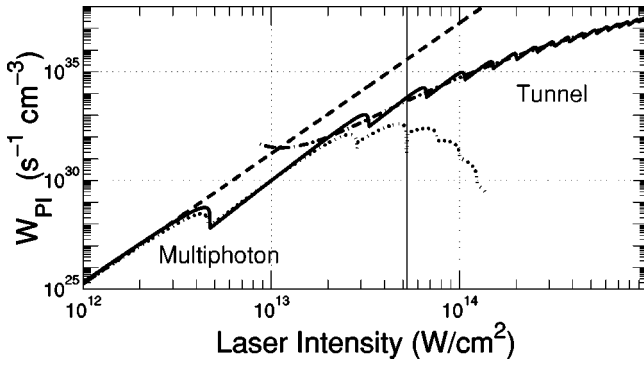


FIG. 2. Ionization rate for fused silica with gap $U_i=9$ eV computed with Keldysh's formulation for multiphoton ionization ($\gamma \gg 1$, dotted curve), tunnel ionization ($\gamma \ll 1$, dash-dotted curve) and from the general formula valid in the intermediate regime (solid line). The background atom density is $2.1 \times 10^{22} \text{ cm}^{-3}$. The multiphoton rate $W_{\text{MPI}} = \sigma_6 I^6 \rho_{\text{at}}$ is shown by the dashed line. The vertical line indicates the maximum intensity reached numerically.

produce the experimental results accurately only with the PI rate given by Eq. (4). Following the same idea, we note that several values for the gap in fused silica may be found in the literature. A gap of 9 eV is found in Refs. 23, 31, 35, 36, 40, and 43. A lower gap of 7.8 eV is found in Refs. 44–46. Recently, a gap of 7.1 eV has been also determined.⁴⁷ Again, we note that we used consistently the gap of 9 eV and the Keldysh formulation for the computation of photoionization rates, since the results computed with a gap of 7.6 eV could not be satisfactorily compared with experiments. A recent paper by Gruzdev⁴⁸ shows, however, that these photoionization rates not only depend on the gap but also on the band structure assumed to be nonparabolic in Keldysh's formulation.

IV. STUDY OF THE TRANSMISSION AS A FUNCTION OF THE PULSE ENERGY

In order to compare the numerical results with experimental data, we first perform two sets of experiments so as to measure the values to be introduced in the code for the nonlinear index of refraction and for the momentum transfer collision time τ_c . The nonlinear refraction index was determined by recording the shift of the nonlinear focus as a function of the laser energy. By comparing measured and calculated transmitted energies as a function of the incident energy of the pulses that are focused in silica, we could determine the momentum transfer collision time τ_c . These two parameters are then kept fixed for the entire analysis. The other physical parameters given above have been obtained from the literature and are kept constant in all numerical simulations.

A. Shift of the nonlinear focus

In a transparent medium with positive nonlinear refraction index, a laser pulse with power above the critical power for self-focusing is known to shrink upon itself along the propagation axis. This leads to an apparent reduction of the focal

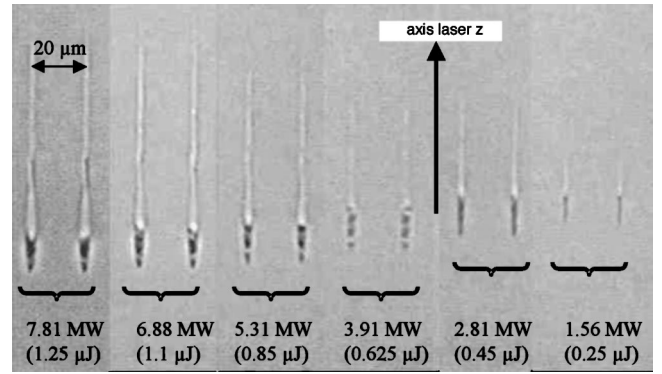


FIG. 3. Observation of the shift of damage tracks in the bulk of a silica sample as a function of the laser energy (indicated in the figure). The pulse duration was 160 fs. The beams were focused in fused silica with an objective 20 \times with NA=0.5.

distance with increasing laser intensity.⁴⁹ In our experiments, the defocusing effect of the plasma generated by the pulse around this nonlinear focus prevents a growth of intensity above a few 10^{13} W/cm^2 . By studying the position of the damage induced by the propagation of laser pulses with different energies under the optical microscope, we could measure the shift of the damage track as a function of the pulse power. The damage tracks shown in Fig. 3 have been obtained by exposing a silica sample during 2 s to 160 fs laser pulses with various energies from $0.25 \mu\text{J}$ (1.56 MW) to $1.25 \mu\text{J}$ (7.8 MW), focused by the objective (20 \times , NA=0.5). The head of the damage moves towards the laser as the pulse energy increases. The damage is assumed to be induced by the plasma, which itself is expected to be triggered around the nonlinear focus. Figure 4 shows the measured shift of the nonlinear focus as a function of the pulse power. The critical power for self-focusing and the nonlinear index of refraction may be deduced from this measurement. An extension of Marburger's formula⁴⁹ has been proposed in a Kerr medium with nonlocal nonlinearity such as the Raman contribution of the Kerr effect.⁵⁰ In this case, the position of the nonlinear focus was shown to be closely reproduced by Eq. (9)

$$z_{\text{nf}} = \frac{0.367 z_R}{\sqrt{[(\max_t \tilde{P}_{\text{in}}(t)/P_{\text{cr}})^{1/2} - 0.852]^2 - 0.0219}}, \quad (9)$$

where $\tilde{P}_{\text{in}}(t)$ indicates how the local power in the temporal slice t is shared between the instantaneous and the delayed component

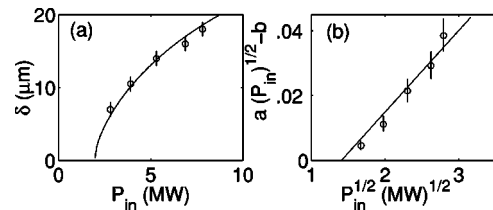


FIG. 4. (a) Shift of the nonlinear focus as a function of the pulse power. The continuous curve corresponds to Eq. (11) after determination of n_2 . (b) Linear representation of the data as in Eq. (12) vanishing for $P_{\text{in}} = P_{\text{cr}}/1.002$.

$$\tilde{P}_{\text{in}}(t) = P_{\text{in}} \left[(1 - f_R) e^{-2(t/t_p)^2} + f_R \int_{-\infty}^t R(\tau - t) e^{-2(\tau/t_p)^2} d\tau \right]. \quad (10)$$

For the parameters given above (pulse duration of $\tau_{FWHM} = 160$ fs), we obtain $\max_t \tilde{P}_{\text{in}}(t) = 1.002 P_{\text{in}}$, a value which is close to P_{in} due to the small fraction of the delayed component. The effective critical power is defined as $P_{\text{cr}}^* \equiv P_{\text{cr}}/1.002$. When a lens prefocuses the laser beam, the shift of the nonlinear focus follows from the lens transformation and reads

$$\delta = \frac{f^2}{f + z_{\text{nf}}}, \quad (11)$$

A function of the shift of the nonlinear focus that must be linear in $\sqrt{P_{\text{in}}}$ reads

$$\sqrt{\frac{P_{\text{in}}}{P_{\text{cr}}^*}} - 1 = -0.148 + \sqrt{0.148^2 + \frac{0.367^2 d \delta^2}{f(f - \delta)^2}}, \quad (12)$$

and is plotted in Fig. 4 as a function of $\sqrt{P_{\text{in}}}$. This function vanishes when $\sqrt{P_{\text{in}}} = 1.4 \text{ MW}^{1/2}$, which corresponds to $\sqrt{P_{\text{cr}}^*}$. Thus, the critical power for self-focusing is $P_{\text{cr}} = 1.98 \text{ MW}$, corresponding to the nonlinear refraction index $n_2 = \lambda_0^2 / 2\pi n_0 P_{\text{cr}} = 3.54 \times 10^{-16} \text{ cm}^2/\text{W}$. These values are in very good agreement with $n_2 = 3.75 \times 10^{-16} \text{ cm}^2/\text{W}$ and $P_{\text{cr}} = 1.72 \text{ MW}$ from Ref. 29. Note also that our specific conditions yield an effective power for self-focusing nearly equal to P_{cr} , due to the rather long pulse durations compared to the characteristic response time for the delayed component in the Kerr term. Our investigation, however, applies quite generally for all types of Kerr media, thus allowing the determination of an effective critical power even when the Raman-Kerr contribution is more important.

B. Study of the transmission

The measurement of the transmission as a function of the incident energy was initially made with the regenerative amplifier laser (800 nm, 160 fs, 200 kHz). Because of its excellent stability, this laser is well adapted for the study of the damage. Because of its high repetition rate (50–250 kHz), it is also well suited for the realization of buried optical elements based on the permanent modification of the refractive index, such as diffraction gratings and waveguides. It provides, however, only a few μJ energy and does not enable us to study the transmission of the laser energy on a wide range. The second Ti:Sapphire laser source produces pulses of 50 fs duration and up to 7 mJ energy, centered around the wavelength 800 nm, at a repetition rate of 1 kHz.

We recorded the transmission of the pulses focused in the silica sample with a microscope objective with NA = 0.5 (20 \times). A lens of high numerical aperture (NA = 0.57) allows us to collect all the transmitted beam. The transmission was measured by a Wattmeter and a calibrated photodiode, as a function of the incident pulse energy. The results of these two measurement techniques for the power are very close and are shown in Fig. 5. The beam attenuation is con-

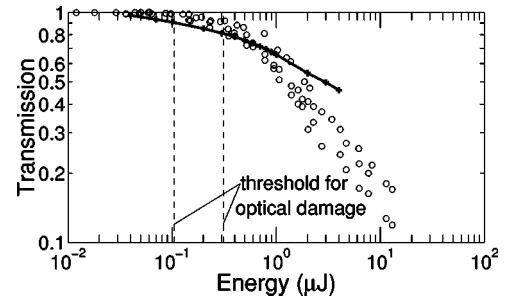


FIG. 5. Transmission as a function of the pulse energy. The central wavelength was 800 nm. The pulse duration and repetition rate were 50 fs (1 kHz) (open circles). The beam was focused in fused silica with a focusing lens (20 \times) with NA = 0.5. The curve marked with crosses indicates the results of numerical simulations. The dashed lines indicate two thresholds for optical damage discussed in the text.

siderable. It reaches almost 90% for pulses of 10 μJ . Note the fast decrease of the transmission when the energy of the incident pulse reaches 4 μJ . The two vertical lines correspond to the onset of damage in bulk silica measured by Sudrie *et al.*⁵¹ The first damage threshold (type I) is associated with a permanent change of refractive index without obvious structural damage. It can be annealed by heating the sample above 900 $^{\circ}\text{C}$ for about 1 hour. The second damage threshold at 0.31 μJ (type II) is accompanied by an induced birefringence in the material around the head of the damage. Under electron microscopy, it reveals a strong material disorder and cannot be cured by heating the sample.

In the literature, the value of the momentum transfer collision time varies from 10^{-15} to 10^{-13} s. We have therefore analyzed the variations of the transmission computed from the numerical code as a function of τ_c . For a 1 μJ pulse focused by an objective (20 \times) with NA = 0.5 in silica, the calculated transmission varies from about 30% with $\tau_c = 10^{-15}$ s to more than 70% with $\tau_c = 10^{-14}$ s. By comparing the transmission resulting from the numerical simulation with the curve of experimentally measured transmission, we obtained the best agreement for the value $\tau_c = 10^{-14}$ s, which we used in all our numerical simulations presented in the following. The analysis of the energy losses in the next section will confirm the dominant role played by avalanche, and related plasma absorption and thus the significant influence of the collision time τ_c on absorption.

Numerical results on the transmission for pulses of 50 fs focused by an objective of microscope (20 \times) with NA 0.5 are indicated by the black crosses in Fig. 5. The comparison between the measured value for the transmission and that calculated by the code is shown in Fig. 5. The calculated onset of absorption is satisfactorily compared with the onset of type I damage at 0.1 μJ . The absorption is correctly reproduced up to values of the order of 1 μJ for the energy of the input pulse. A change of slope in the transmission signaling the onset of an additional mechanism occurs around 0.4 μJ , close to the type II damage threshold (appearance of irreversible damage).^{14,52} With higher energy, simulations significantly overestimate the transmission obtained in the experiments. This discrepancy is not explained by the pres-

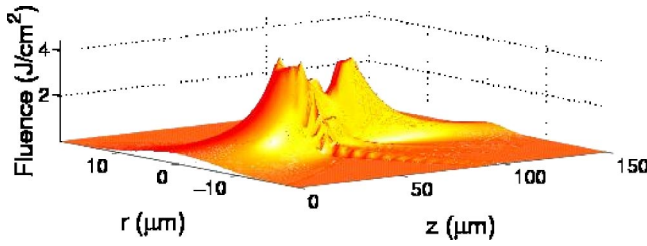


FIG. 6. Numerically computed fluence as a function of the propagation distance. Pulse 800 nm, 160 fs, 1.1 μJ . Objective 20 \times with NA=0.5.

ence of an electron plasma alone, though the latter might be important in triggering physical effects and absorption occurring over longer times. An additional attenuation mechanism therefore occurs, which the code does not take into account. We study this mechanism in Sec. VI. As already mentioned, the decay constant in our model is only valid for the description of an electron-hole plasma.

V. DETAILED STUDY OF THE NUMERICAL RESULTS AND COMPARISON WITH THE EXPERIMENT

We have analyzed in detail the numerical results concerning the propagation and compared them with experimental results. The experimentally accessible quantity is the fluence distribution defined as $F \equiv \int_{-\infty}^{+\infty} |E|^2 dt$. Figure 6 is a representation in three dimensions of the fluence along the propagation axis for a 1.1 μJ pulse.

Figure 7 shows the fluence as a function of the propagation distance of the laser pulse from the entrance surface of the sample, for two different energies, 0.45 and 1.1 μJ . The FWHM of the fluence at each position is shown by the dashed curve and represents the beam focusing, followed by a defocusing stage due to the plasma generated by photoionization and avalanche. For an energy of 1.1 μJ , the beam propagates beyond the nonlinear focus with a weak diffraction angle. Thus, the numerical simulation predicts a laser

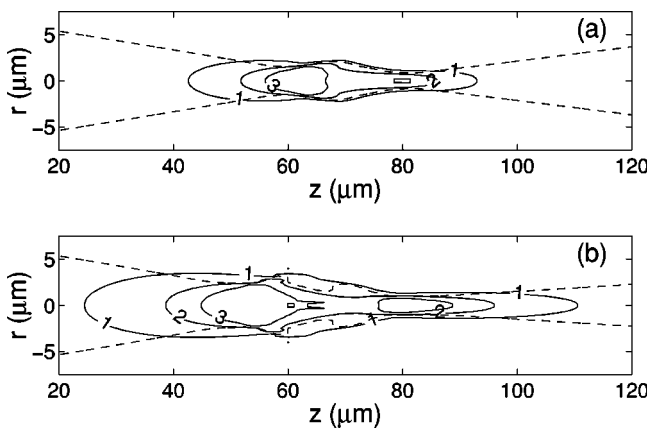


FIG. 7. Beam diameter in dashed curve (FWHM of the fluence at each propagation distance) and various levels of the fluence distribution (continuous contours for 1, 2, and 3 J/cm^2 as a function of z). Pulse: 800 nm, 160 fs. Focusing lens 20 \times with NA=0.5). (a) 0.45 μJ . (b) 1.1 μJ .

filamentation in spite of the tight focusing of the pulse (which is usually expected to induce breakdown). The 1.1 μJ pulse is defocused before the 0.45 μJ pulse, indicating that the plasma generated by the 1.1 μJ pulse is formed before that generated by the 0.45 μJ pulse. The flux takes the shape of an elongated filament (Fig. 7). For an incident pulse energy of 0.45 μJ , the domain where the flux exceeds 1 J/cm^2 extends from 45 to 90 μm and, for a 1.1 μJ pulse, it extends from 25 to 110 μm . The length of the tracks observed with the optical microscope (see Fig. 3) are 43 and 85 μm at these energies, showing quite good agreement with the lengths of the elongated filaments in Fig. 7.

Figure 8 shows the peak intensity as a function of the propagation distance obtained for pulses with six different energies from 0.25 to 1.25 μJ . For energies up to 2 μJ , the maximum intensity is $5 \pm 0.5 \times 10^{13} \text{ W}/\text{cm}^2$. It decreases when the energy of the input beam decreases. This intensity is in a range described by the tunnel ionization (Fig. 2). Keldysh's formulation for multiphoton ionization and *a fortiori* the simplified multiphoton ionization rate scaling as I^K cannot be used in these focusing conditions. These results on the laser intensities corroborate our choice of the general Keldysh's formulation for the description of the ionization rate.

Figure 9 shows the electron density on the propagation axis ($r=0$) for the same pulse energies as in Fig. 8. For these energies, the maximum electron density is clamped between 2×10^{20} and $4 \times 10^{20} \text{ cm}^{-3}$. This saturation occurs when the plasma defocusing of the laser beam locally balances the optical Kerr effect. For the pulses we use (800 nm, 1 μJ , 160 fs, objective 20 \times with NA=0.5), this occurs in silica for an electron density of about 2 to $4 \times 10^{20} \text{ cm}^{-3}$. Even under such strong focusing conditions, the intensity cannot grow sufficiently to obtain electron densities higher than $4 \times 10^{20} \text{ cm}^{-3}$.

Figure 10 illustrates the time evolution of free-carrier generation. When avalanche is neglected, they are produced by optical field ionization on the ascending part of the pulse (dashed curve). Near the peak of the pulse intensity shown by the dash-dotted curve, avalanche suddenly comes into play and generates additional electrons, increasing the density by more than 1 decade (solid curve).

In order to determine the electron density prevailing at the appearance of the structural damage (type II) in silica, the shift of various electron density levels from 10^{19} to $4 \times 10^{20} \text{ cm}^{-3}$ was computed and compared with the shift of the damage track observed in experiments. The electron density for which the shift corresponds to our experimental measurements is about $2 \times 10^{20} \text{ cm}^{-3}$, indicating that the type II damage is formed when an electron density larger than $2 \times 10^{20} \text{ cm}^{-3}$ is reached.

In order to confirm this condition on the electron density for the appearance of the damage, we compared the corresponding contour with the lateral and longitudinal dimensions of the damage. To perform a quantitative comparison, the resolution of the images of the damage was improved by using a scanning electron microscope (SEM), which allows the observation of details smaller than 10 nm.

Figure 11 shows in parallel an image of a structural damage induced in silica and the levels of the electron density

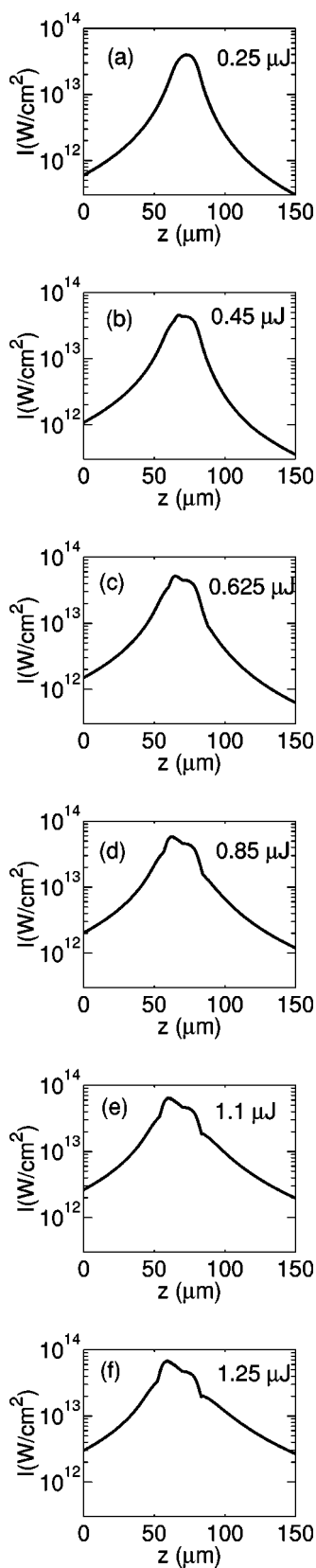


FIG. 8. Numerically computed intensity as a function of the propagation distance. Objective ($20\times$) with $\text{NA}=0.5$. Pulse 800 nm, 160 fs. The different pulse energies of the experiments are indicated in each figure.

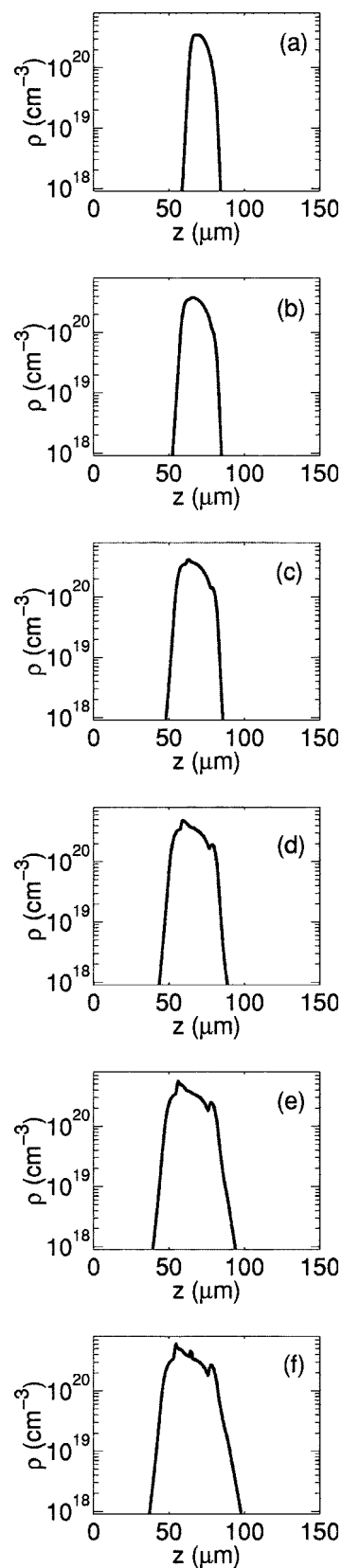


FIG. 9. Numerically computed electron density on the propagation axis. Pulse: 800 nm, 160 fs. Focusing lens $20\times$ with $\text{NA} 0.5$. (a) 0.25 μJ . (b) 0.45 μJ . (c) 0.625 μJ . (d) 0.85 μJ . (e) 1.1 μJ . (f) 1.25 μJ .

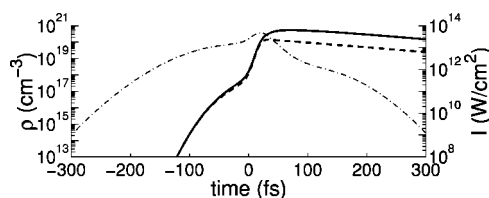


FIG. 10. Numerically computed electron density (scale on the left axis) as a function of time for an input pulse of $1 \mu\text{J}$. Here, the propagation distance is $57 \mu\text{m}$. The solid curve shows the electron density when avalanche is taken into account. The dashed curve represents its counterpart when avalanche is neglected. The dash-dotted curve represents the pulse intensity (scale on the right axis) at $z=57 \mu\text{m}$.

computed in the numerical simulations. The damage consists of two distinct parts. There is initially a first zone, very fractured, of a few μm width and of a few tens of μm length. A permanent induced birefringence is observed around the head of this fracture zone, as discussed in Ref. 53. Following this first large damage zone, a second very narrow damage of about 200 to 300 nm can be distinguished, which we will call the tail of the optical damage.

The image of the damage tracks and the representation of the electron density have the same spatial scales so as to compare easily transverse and longitudinal dimensions of the principal damage with those of the generated plasma. The size of the plasma with an electron density exceeding 10^{20} cm^{-3} is very close to the size of the damage: The transverse width and the longitudinal length of the principal damage are $3.7 \pm 0.5 \mu\text{m}$ and $25 \pm 4 \mu\text{m}$, respectively. The transverse width and the longitudinal length of the region where the plasma of density exceeds 10^{20} cm^{-3} are $4.3 \pm 0.5 \mu\text{m}$ and $28 \pm 1 \mu\text{m}$, respectively. More generally, the shape and the dimensions of the domain where the plasma density exceeds 10^{20} cm^{-3} reproduce well those of the first damage zone. From these results, the first damage track corresponds to type II damage and is associated with the generation of an electron-ion plasma.

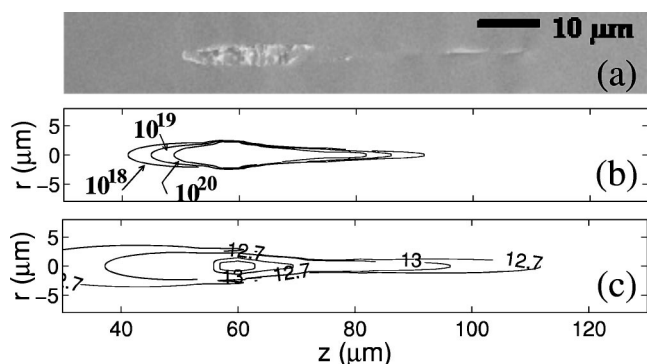


FIG. 11. Comparison between experiments and simulation. (a) Image from electron microscope of a damage track obtained by focusing pulses in fused silica (800 nm, 160 fs, $1 \mu\text{J}$. Objective $20\times$ with $\text{NA}=0.5$). (b) Numerical simulation: The curves bound regions where the electron density exceeds the level 10^{18} , 10^{19} , or $10^{20} \text{ e}^-/\text{cm}^3$. Parameters as in the experiments. (c) Computed intensity contourplots. The labels 12.7 and 13 in (c) indicate 5×10^{12} and $10^{13} \text{ W}/\text{cm}^2$.

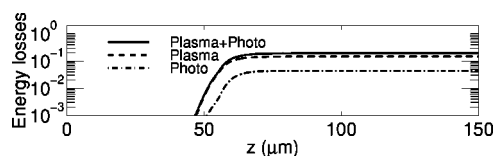


FIG. 12. Numerical simulation: Energy losses as a function of the propagation distance. Pulse 800 nm, $1.1 \mu\text{J}$, 160 fs. Focusing lens $20\times$ with $\text{NA}=0.5$. Losses due to plasma absorption (dashed curve), optical field absorption (dash-dotted curve), and both processes (continuous curve).

Both our measurements and the simulations for the transmission of the power after the first damage zone show that it still exceeds the critical power for self-focusing. A beam refocusing is thus expected. The very narrow tail of type II damage observed around $100 \mu\text{m}$ in Fig. 11(a) is thus possibly due to a second self-focusing. As shown in Fig. 6, the calculated fluence in the center of the beam exhibits a second peak 30 to $40 \mu\text{m}$ after the first one. The appearance of the filamentary track could be linked to this refocusing peak. We interpret this tail as a type II damage embedded in a type I damage visible in Fig. 3. However, the results of our code do not show the formation of this new nonlinear focus. In this respect, the measured transverse dimension of the tail track ($\leq 200 \text{ nm}$) is not compatible with the range of validity of the nonlinear envelope equation solved by the code.

Recent studies were also made on the self-guided propagation inducing damage.⁵⁴ Experimental results close to our results were obtained. For example, pulses with energies from 0.3 to $0.5 \mu\text{J}$ focused with an objective of numerical aperture $\text{NA}=0.3$ were shown to induce damage with a diameter of $1.7 \mu\text{m}$ and lengths between 20 and $40 \mu\text{m}$.

The appearance of the damage is often associated with the avalanche process. It is thus instructive to compare the role played by optical field ionization to the role of avalanche. To this aim, we compare the energy losses due to plasma absorption (linked to the avalanche process) with the energy losses due to optical field ionization. Figure 12 gives the total energy losses (absorption due to optical field ionization and losses by avalanche) for a pulse of $1.1 \mu\text{J}$ and 160 fs focused in silica by an objective $20\times$ with $\text{NA}=0.5$. For a comparison, Fig. 13 shows the electron density computed from optical field ionization only and for both ionization processes, optical field and avalanche. Significant losses begin for densities about 10^{19} cm^{-3} . The losses are primarily due to plasma absorption for the five simulated energies. This ex-

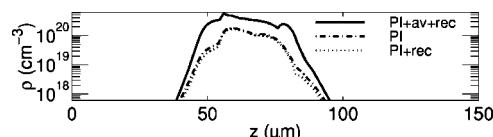


FIG. 13. Numerical simulation: Electron density as a function of the propagation distance. Pulse 800 nm, $1.1 \mu\text{J}$, 160 fs. Focusing lens $20\times$ with $\text{NA}=0.5$. The electron density generated by photoionization (PI) only is plotted by the dash-dotted curve. The dotted curve shows the electron density obtained by PI and recombination (rec), and the continuous curve shows the density obtained by photoionization, avalanche, and recombination.

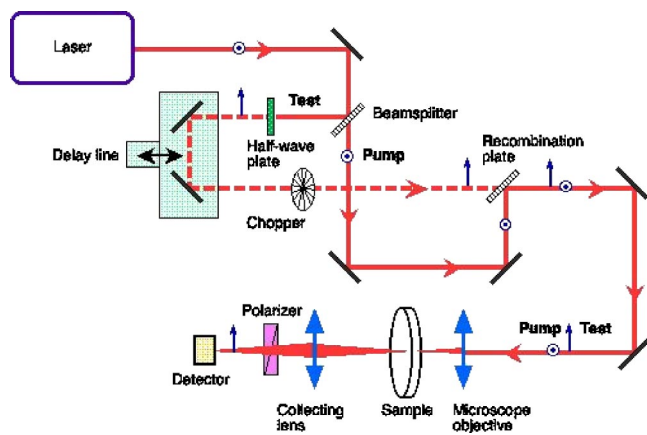


FIG. 14. General scheme of the pump-probe experiment in transmission.

plains the observations of Sec. IV B concerning the strong influence of the characteristic time for collision τ_c on the transmission.

The presence of free electrons is necessary to initiate the avalanche process. Optical field ionization generates the first electrons. As shown in Fig. 13, optical field ionization is the prevailing effect for electron densities lower than 10^{18} cm^{-3} . Avalanche contributes significantly to ionization when larger densities are reached. At the maximum of the electron density, 30% of the electrons were generated by optical field ionization and 70% by avalanche. With collimated beams, the balance between self-focusing and plasma defocusing was shown to lead to a saturation of the electron density around 10^{19} cm^{-3} (see Ref. 15). The tight focusing of the beam in silica triggers the avalanche process, which saturates self-focusing for electron densities larger than 10^{20} cm^{-3} . These results indicate that type II irreversible damage in silica is closely related to avalanche. However, the maximum electron density remains about one order of magnitude below the critical density, $\rho_c \equiv \omega_0^2 \epsilon_0 m^* / e^2 = 1.74 \times 10^{21} \text{ cm}^{-3}$.

VI. DETERMINATION OF THE TRANSMISSION WITH TWO PULSES

A. Measurements of the transmission of the probe

The calculated transmissions exceed the values measured for energies larger than $1 \mu\text{J}$. From this observation, we conclude that there is an additional attenuation mechanism which is not taken into account in the simulations. In order to obtain information on this new mechanism, we carried out pump-probe experiments. The pulse was split into a pump pulse and a weaker probe pulse. The delay between both pulses could be modified by a delay line. The general outline of the experiment is given by Fig. 14.

Pump-probe and pump-pump experiments were carried out with colinear beams focused spatially at the same point by the same objective of microscope (growth $20\times$ with $\text{NA}=0.5$). The control camera placed after the sample allows both ways to overlap at the focus of the objective. This overlap is then improved so as to increase to its maximum the

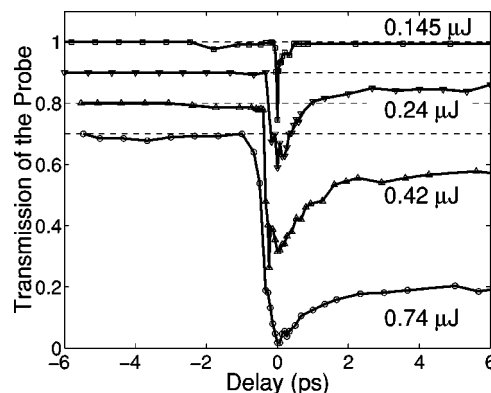


FIG. 15. Results of the pump-probe experiments in fused silica. Focusing lens $20\times$ with $\text{NA}=0.5$. Probe pulse: 800 nm , $0.025 \mu\text{J}$, 50 fs , 1 kHz with modulation. Pump pulse: 800 nm , 50 fs , 1 kHz . The pump energies are $0.145 \mu\text{J}$ (squares), $0.24 \mu\text{J}$ (triangles down), $0.42 \mu\text{J}$ (triangles up), and $0.74 \mu\text{J}$ (circles). The three curves with largest energies have been shifted for clarity. The dashed lines indicate the shifts.

absorption of the probe for a zero delay between pump and probe.

When the delay between the pump and probe pulses is zero, circular fringes (of equal inclination) are observed. In order to avoid strong instabilities generated by these interferences on the detected signal, a half-wave plate is placed on the way of the probe pulse at 45° of the polarization of the beam so as to obtain a polarization perpendicular to that of the pump pulse. The interferences which appear for a zero delay between both pulses disappear. The instabilities they caused are then strongly reduced.

A repetition rate different from that of the pump signal was imposed on the probe signal by mechanically chopping the beam. The synchronization detector connected to the chopper receives the signal of the diode and detects only the signal with the frequency of the chopper. Thus, only the absorption of the probe pulse due to the plasma generated by the pump pulse is detected.

Differential measurements of the transmission were performed with the laser source (1 kHz , 50 fs).

Figure 15 shows the results obtained from pump-probe experiments as a function of delay between pump and probe pulses for four pump pulse energies. The probe pulses have an energy much lower than the damage threshold and therefore do not modify the material by themselves.

B. Discussion of the results of pump-probe experiments

Three regimes can be distinguished from the results obtained in pump-probe experiments. (i) When the energy of the pump pulse is lower than the first damage threshold, there is no induced absorption signal. In our experiments with pulses focused by an objective $20\times$ with $\text{NA}=0.5$, the type I damage threshold is about $0.1 \mu\text{J}$. It is therefore entirely consistent with the absence of a plasma generated at these pump energies as predicted by the code. (ii) When the energy of the pump is equal to or slightly larger than the damage threshold, a fast signal is observed, characteristic of

the generation of an electron-hole plasma. The lifetime of this plasma is around 150 fs. It is taken into account by the introduction of the term $-\rho/\tau_r$ into Eq. (6) for the evolution of the electron density. The value of $\tau_r=150$ fs used in our numerical simulations corresponds to our experimentally determined value as well as that of Audebert *et al.* and Tien *et al.*^{37,42} (iii) For higher pump energies, in addition to the short-lived component, a temporal shift towards negative delays and a long duration signal becomes apparent. The temporal shift is well explained by the splitting of the pump pulse and the advance of the leading pulse in the plasma it generates.¹⁵ Consistently, the shift increases when the pump pulse energy increases. The long-duration signal appears when the energy of the pump pulse is sufficient to generate an electron-ion plasma by avalanche. This electron-ion plasma induces permanent structural damage of type II. We carried out complementary experiments showing that this absorption is still present several ns after the passage of the pump pulse. It is obvious that the electron-hole plasma cannot be responsible for this long absorption. The presence of an electron-ion plasma alone does not explain this effect. At $0.25\ \mu\text{J}$ the generated density of the electron-ion plasma already overcomes that of the electron-hole plasma ($7 \times 10^{19}\ \text{cm}^{-3}$ for a total of $2 \times 10^{20}\ \text{cm}^{-3}$). The electron-ion plasma, however, might seed the conditions for triggering other physical effects responsible for the long-time absorption that is not reproduced by the model.

We do not yet have an interpretation of this long absorption. The induced absorption lasts for increasingly longer times when the energy of the pump pulse increases. The same type of absorption in silica was observed and published by Martin *et al.*⁵⁵ They suppose that this long absorption is due to the presence of metastable defects in silica such as self-trapped excitons. Yamada *et al.*⁵⁴ also report on the influence of the duration of the exposures on the appearance of the damage. In addition, similar experiments that we performed in a quartz crystal show a clear reduction of this long signal in the crystalline form. These observations lead us to suggest that this long-time absorption might be of thermal origin. It could correspond, for example, to a molten phase of material at very high temperature. Von der Linde *et al.*⁵⁶

show in particular that ablation by pulses of duration of about 100 fs can be interpreted in terms of transient thermal processes. The increase in the duration of this absorption with the pump laser energy could be explained by an increase of the heated volume. A thermal process would also explain the weaker absorption in crystalline quartz because of its higher thermal conductivity. Additional experiments with lasers working at a lower repetition rate will be necessary to fully understand this phenomenon.

VII. CONCLUSION

In this paper, we have carried out an extensive study of the propagation of infrared femtosecond laser pulses tightly focused in fused silica. Integrated beam transmittance, time-resolved pump probe transmission experiments, as well as the characterization of permanent damages have been carried out as a function of input pump pulse energy. These results have been compared to numerical simulations of the propagation and absorption of the pulse. The results reveal a filamentary propagation regime. Two types of damage are observed. Type I damage is associated with a permanent change of refractive index induced by the generation of an electron-hole plasma. In this case the avalanche process does not contribute to ionization. The dimensions of the damage tracks are well reproduced by the dimensions of the domain, where the computed fluence exceeds $1\ \text{J}/\text{cm}^2$. Measurements of the plasma lifetime show that it is short-lived. We attribute this type I damage to the fast capture of electrons by trap centers in the disordered medium, giving rise to a metastable change of the polarizability of the medium.⁵⁷ The second type of damage is structural. It occurs when the avalanche process becomes effective. Numerical results are in good agreement with the observed type II damage. Comparison of the shape and location of this damage with contour plots of the computed electron density allows us to determine the density at which it occurs. This value is 1 decade below the critical plasma density. Appearance of an additional absorption of long duration is associated with this damage. We interpret this as a transition from an electron-hole plasma to an electron-ion plasma.

¹M. Lenzner, J. Krüger, W. Kautek, and F. Krausz, *Appl. Phys. A: Mater. Sci. Process.* **A68**, 369 (1999).

²K. M. Davis, K. Miura, N. Sugimoto, and K. Hirao, *Opt. Lett.* **21**, 1729 (1996).

³D. Homoelle, S. Wielandy, A. L. Gaeta, N. F. Borrelli, and C. Smith, *Opt. Lett.* **24**, 1311 (1999).

⁴C. B. Schaffer, A. Brodeur, J. F. Garcia, and E. Mazur, *Opt. Lett.* **26**, 93 (2001).

⁵F. H. Loesel, J. P. Fischer, M. H. Götz, C. Horvath, T. Juhasz, F. Noack, N. Suhm, and J. F. Bille, *Appl. Phys. B: Lasers Opt.* **B66**, 121 (1998).

⁶E. N. Glezer, M. Milosavljevic, L. Huang, R. J. Finlay, T.-H. Her, J. P. Callan, and E. Mazur, *Opt. Lett.* **21**, 2023 (1996).

⁷M. Watanabe, H.-B. Sun, S. Juodkazis, T. Takahashi, S. Matsuo,

Y. Suzuki, J. Nishii, and H. Misawa, *Jpn. J. Appl. Phys., Part 2* **37**, L1527 (1998).

⁸K. Miura, J. Qui, H. Inouye, T. Mitsuyu, and K. Hirao, *Appl. Phys. Lett.* **71**, 3329 (1997).

⁹K. Hirao and K. Miura, *Jpn. J. Non-Cryst. Solids* **239**, 91 (1998).

¹⁰T. Toma, Y. Furuya, W. Watanabe, J. Nishii, K. Hayashi, and K. Itoh, *Opt. Rev.* **7**, 14 (2000).

¹¹Y. Kondo, K. Nouchi, T. Mitsuyu, M. Watanabe, P. G. Kazansky, and K. Hirao, *Opt. Lett.* **24**, 646 (1999).

¹²H.-B. Sun, Y. Zu, S. Matsuo, and H. Misawa, *Opt. Rev.* **6**, 396 (1999).

¹³D. Von der Linde and H. Schüller, *J. Opt. Soc. Am. B* **13**, 216 (1996).

¹⁴L. Sudrie, A. Couairon, M. Franco, B. Lamouroux, B. Prade, S.

- Tzortzakis, and A. Mysyrowicz, Phys. Rev. Lett. **89**, 186601 (2002).
- ¹⁵S. Tzortzakis, L. Sudrie, M. Franco, B. Prade, A. Mysyrowicz, A. Couairon, and L. Berge, Phys. Rev. Lett. **87**, 213902 (2001).
- ¹⁶M. Mlejnek, E. M. Wright, and J. V. Moloney, Opt. Lett. **23**, 382 (1998).
- ¹⁷A. Couairon, G. Méchain, S. Tzortzakis, M. Franco, B. Lamouroux, B. Prade, and A. Mysyrowicz, Opt. Commun. **225**, 177 (2003).
- ¹⁸Q. Feng, J. V. Moloney, A. C. Newell, E. M. Wright, K. Cook, P. K. Kennedy, D. X. Hammer, B. A. Rockwell, and C. R. Thompson, IEEE J. Quantum Electron. **33**, 127 (1997).
- ¹⁹M. Kolesik, E. M. Wright, and J. V. Moloney, Phys. Rev. Lett. **92**, 253901 (2004).
- ²⁰A. Dubietis, E. Gaizauskas, G. Tamosauskas, and P. Di Trapani, Phys. Rev. Lett. **92**, 253903 (2004).
- ²¹T. Brabec and F. Krausz, Phys. Rev. Lett. **78**, 3282 (1997).
- ²²M. Kolesik, G. Katona, J. V. Moloney, and E. M. Wright, Phys. Rev. Lett. **91**, 043905 (2003).
- ²³M. R. Junnarkar, Opt. Commun. **195**, 273 (2001).
- ²⁴A. L. Gaeta, Phys. Rev. Lett. **84**, 3582 (2000).
- ²⁵R. H. Stolen, J. P. Gordon, W. J. Tomlison, and H. A. Haus, J. Opt. Soc. Am. B **6**, 1159 (1989).
- ²⁶G. L. K. Wong and Y. R. Shen, Phys. Rev. A **10**, 1277 (1974).
- ²⁷A. A. Zozulya, S. A. Diddams, A. G. Van Engen, and T. S. Clement, Phys. Rev. Lett. **82**, 1430 (1999).
- ²⁸A. A. Zozulya, S. A. Diddams, and T. S. Clement, Phys. Rev. A **58**, 3303 (1998).
- ²⁹R. W. Boyd, *Nonlinear Optics* (Academic, London, 1992).
- ³⁰E. Yablonovitch and N. Bloembergen, Phys. Rev. Lett. **29**, 907 (1972); N. Bloembergen, IEEE J. Quantum Electron. **QE-10**, 375 (1974).
- ³¹B. C. Stuart, M. D. Feit, S. Herman, A. M. Rubenchik, B. W. Shore, and M. D. Perry, Phys. Rev. B **53**, 1749 (1996).
- ³²B. C. Stuart, M. D. Feit, S. Herman, A. M. Rubenchik, B. W. Shore, and M. D. Perry, J. Opt. Soc. Am. B **13**, 459 (1996).
- ³³Z. Wu, H. Jiang, Q. Sun, H. Yang, and Q. Gong, Phys. Rev. A **68**, 063820 (2003).
- ³⁴L. V. Keldysh, Sov. Phys. JETP **20**, 1307 (1965) [Zh. Eksp. Teor. Fiz. **47**, 1945 (1964)].
- ³⁵B. C. Stuart, M. D. Feit, A. M. Rubenchik, B. W. Shore, and M. D. Perry, Phys. Rev. Lett. **74**, 2248 (1995).
- ³⁶M. Li, S. Menon, J. P. Nibarger, and G. N. Gibson, Phys. Rev. Lett. **82**, 2394 (1999).
- ³⁷P. Audebert, Ph. Daguzan, A. Dos Santos, J. C. Gauthier, J. P. Geindre, S. Guizard, G. Hamoniaux, K. Krastev, P. Martin, G. Petite, and A. Antonetti, Phys. Rev. Lett. **73**, 1990 (1994).
- ³⁸B. Rethfeld, Phys. Rev. Lett. **92**, 187401 (2004).
- ³⁹A. Kaiser, B. Rethfeld, M. Vicanek, and G. Simon, Phys. Rev. B **61**, 11 437 (2000).
- ⁴⁰M. V. Fischetti, D. J. Di Maria, S. D. Brorson, T. N. Theis, and J. R. Kirtley, Phys. Rev. B **31**, 8124 (1985).
- ⁴¹M. Abramowitz and I. A. Stegun, *Handbook of Mathematical Functions* (Dover, New York, 1972).
- ⁴²A.-C. Tien, S. Backus, H. Kapteyn, M. Murnane, and G. Mourou, Phys. Rev. Lett. **82**, 3883 (1999).
- ⁴³M. Lenzner, J. Krüger, S. Sartania, Z. Cheng, Ch. Spielmann, G. Mourou, W. Kautek, and F. Krausz, Phys. Rev. Lett. **80**, 4076 (1998).
- ⁴⁴P. Liu, W. L. Smith, H. Lotem, J. H. Bechtel, N. Bloembergen, and R. S. Adhav, Phys. Rev. B **17**, 4620 (1978).
- ⁴⁵P. Liu, R. Yen, and N. Bloembergen, Appl. Opt. **18**, 1015 (1979).
- ⁴⁶V. Nathan, A. H. Guenther, and S. S. Mitra, J. Opt. Soc. Am. B **2**, 294 (1985).
- ⁴⁷A. P. Joglekar, H. Liu, G. J. Spooner, E. Meyhöfer, G. Mourou, and A. J. Hünig, Appl. Phys. B: Lasers Opt. **B77**, 25 (2003).
- ⁴⁸V. E. Gruzdev, J. Opt. Technol. **71**, 504 (2004).
- ⁴⁹J. H. Marburger, Prog. Quantum Electron. **4**, 35 (1975).
- ⁵⁰A. Couairon, Eur. Phys. J. D **27**, 159 (2003).
- ⁵¹L. Sudrie, M. Franco, B. Prade, and A. Mysyrowicz, Opt. Commun. **171**, 279 (1999).
- ⁵²L. Sudrie, M. Franco, B. Prade, and A. Mysyrowicz, Opt. Commun. **191**, 333 (2001).
- ⁵³B. Poumellec, L. Sudrie, M. Franco, B. Prade, and A. Mysyrowicz, Opt. Express **11**, 1070 (2003).
- ⁵⁴K. Yamada, W. Watanabe, T. Toma, K. Itoh, and J. Nishii, Opt. Lett. **26**, 19 (2001).
- ⁵⁵P. Martin, S. Guizard, Ph. Daguzan, G. Petite, P. D'Oliveira, P. Meynadier, and M. Perdrix, Phys. Rev. B **55**, 5799 (1997).
- ⁵⁶D. Von der Linde and K. Sokolowski-Tinten, Appl. Surf. Sci. **154-155**, 1 (2000).
- ⁵⁷A. M. is indebted to N. Bloembergen for an illuminating discussion.